International Journal of Multiphase Flow 187 (2025) 105179

Contents lists available at ScienceDirect

International Journal of Multiphase Flow

journal homepage: www.elsevier.com/locate/ijmulflow

ML-based semantic segmentation for quantitative spray atomization description

Basil Jose [a], Oliver Lammel [b], Fabian Hampp [a],*

[a] *Institute of Combustion Technology for Aerospace Engineering, University of Stuttgart, Pfaffenwaldring 38-40, 70569 Stuttgart, Germany*
[b] *Institute of Combustion Technology, German Aerospace Center (DLR), Pfaffenwaldring 38-40, 70569 Stuttgart, Germany*

ARTICLE INFO

Dataset link: https://doi.org/10.18419/DARUS-4739

Keywords:
Primary atomization
Gas-liquid-interface interactions
Machine learning
Semantic spray segmentation
Technical sprays
Liquid fuel combustion

ABSTRACT

Fuel spray atomization in gas turbine systems significantly impacts the combustion process and thereby emission formation. Considering the necessity for quantitative description of the influence of operating conditions on the spray breakup mechanisms, a machine learning (ML) based methodology is introduced to accurately segment the dispersed liquid from the continuous gaseous phase in shadowgraphy images. The segmented images subsequently facilitate a high-level statistical analysis of gas-liquid-interface contours and ultimately instability dynamics. For this purpose, multiple ML models varying in architecture (Semantic FPN and DeepLabV3+), datasets and augmentations are benchmarked to achieve the best performance. Subsequently, the best model is validated and used to obtain conditional statistics on the detected spray contours of three different spray types (jet-in-crossflow, pressure swirl spray and prefilming airblast spray). The model showcases high robustness, transferability across spray configurations and accuracy along multiple never-seen sprays thereby illustrating the superiority of deep learning methods for scientific image segmentation tasks. Moreover, the inferred high-level statistical analysis provides novel quantitative insights into the involved turbulence-spray interactions aiding the understanding of jet, sheet and film atomization under highly turbulent flow conditions.

1. Introduction

Fuel spray atomization processes, entailing the disintegration of liquid jets, films, or sheets into ligaments and fine droplets, play a pivotal role in the performance and achievable emission standards in combustion processes. Inadequate atomization can lead to larger droplets that, in turn, result in reduced evaporation rates and thereby impede mixture homogenisation (Hampp et al., 2023). Related mixture stratification can influence the formation of soot in fuel-rich and NO_X in fuel-lean regions with elevated initial temperatures (Chong and Hochgreb, 2014; Enagi et al., 2019). With the transition to green and sustainable fuels, the fuel flexibility requirements of future injection and combustion systems are increasing accordingly. For liquid fuel gas turbine combustion across all sectors, this spans from traditional hydrocarbons, biofuels, oxygenated fuels, and sustainable aviation fuels to ammonia (Anderson et al., 2020; Stefanizzi et al., 2021; Molière, 2023). This inherently involves wide variability in terms of physical (e.g. viscosity, surface tension, phase change behaviour) and chemical properties (e.g. reactivity, aromatic content). It is well known that physical fuel properties such as viscosity and surface tension can strongly influence both primary and secondary atomization (Lefebvre and McDonell, 2017). Consequently, atomizer performance and fuel flexibility are particularly pertinent for future gas turbine combustion systems. The most common atomizer types for such purposes are arguably multi-hole jet-in-crossflow (JiCF), variants of pressure swirl (PS), and airblast injection systems (Lindman et al., 2014; Raghu et al., 2015). In the former two technologies, pressure is converted into kinetic energy, driving the disintegration of the liquid jets or PS sheets. Frequently, these systems are subjected to gaseous oxidiser cross- or coflow that excite Kelvin–Helmholtz instabilities on the gas-liquid-interface surface (Chong et al., 2012; Oshima and A., 2019; Petry et al., 2022). In airblast systems, typically high shear stresses within the gaseous flow govern the atomization of liquid films. Thus, the interaction of the liquid spray and the turbulent oxidiser flow in its proximity governs the atomization process, fuel placement and thereby atomizer performance (Koyama and Tachibana, 2012; Kang et al., 2024). Enhanced fundamental understanding, in particular at high Reynolds number (Re), of the involved processes is indispensable.

Detailed characterisation of atomization and fuel/oxidiser mixture formation is essential for the development of future injector technologies. Spherical droplet size can accurately be measured using techniques such as phase Doppler interferometry (PDI), laser-induced fluorescence (LIF) and Mie scattering ratios (Fansler and Parrish, 2015).

---

* Corresponding author.
E-mail address: fabian.hampp@ivlr.uni-stuttgart.de (F. Hampp).

https://doi.org/10.1016/j.ijmultiphaseflow.2025.105179
Received 1 November 2024; Received in revised form 6 February 2025; Accepted 11 February 2025

Nomenclature

α	Mass flow rate ratio $\left(\alpha = \frac{\dot{m}_l}{\rho_g\, A\, u_b}\right)$
A	Cross-sectional area of the flow channel [mm^2]
$\mathcal{A}_1$	Pixel accuracy for the spray class
d_h	Hydraulic (nozzle) diameter [mm]
d_l	Injector orifice diameter [mm]
$\mathcal{J}_1$	Jaccard index for the spray class
$\overline{\mathcal{J}}$	Mean Jaccard index (across all classes)
$\mathcal{J}_{\mathrm{B},1}$	Boundary Jaccard index for the spray class
κ	Instantaneous curvature of the GLI [mm^{-1}]
$\overline{\kappa}$	Mean curvature of the GLI [mm^{-1}]
κ'	Fluctuation of the GLI curvature [mm^{-1}]
l_b	Length of the continuous sheet prior to breakup [mm]
l_{max}	Maximum penetration depth of the detached liquid film [mm]
l_{min}	Minimum penetration depth of the detached liquid film [mm]
$\bar{l}$	Mean penetration depth of the detached liquid film [mm]
l_s	Length of the continuous (unrolled) jet prior to breakup [mm]
l_x	Jet penetration length in the x-direction [mm]
l_y	Jet penetration length in the y-direction [mm]
$\dot{m}_l$	Liquid (fuel or water) mass flow rate [g/s]
μ_l	Liquid (fuel or water) dynamic viscosity [Pa s]
μ_g	Gas (air) dynamic viscosity [Pa s]
N	Number of instantaneous images
ΔP_l	Pressure drop across the liquid injector [bar]
q	Momentum flux ratio $\left(q = \frac{\rho_l\, u_l^2}{\rho_g\, u_b^2}\right)$
r_a	Disturbance amplitude on the GLI [mm]
$\overline{r_a}$	Mean disturbance amplitude on the GLI [mm]
r_a'	Standard deviation of the GLI disturbance amplitude [mm]
r_b	Radial component of sheet prior to breakup [mm]
r_s	Radial displacement of the instantaneous GLI [mm]
$\overline{r_s}$	Mean radial displacement of the GLI [mm]
r_s'	Standard deviation of the GLI displacement [mm]
ρ_l	Liquid (fuel or water) density [kg/m^3]
ρ_g	Gas (air) density [kg/m^3]
R_e	Reynolds number
Re_g	Gas-phase Reynolds number $\left(Re_g = \frac{\rho_g\, u_b\, d_l}{\mu_g}\right)$
Re_l	Liquid (fuel or water) jet Reynolds number $\left(Re_l = \frac{\rho_l\, u_l\, d_l}{\mu_l}\right)$
s_i	Instantaneous GLI contour
s_{th}	Instantaneous theoretically undisturbed GLI
σ	Liquid (fuel or water) surface tension [N/m]
T_g	Gas (air) temperature [K]
T_w	Air wall film temperature [K]
θ_s	Instantaneous half-spray cone angle [°]
Θ_s	Instantaneous full-spray cone angle [°]
u_a	Atomization (airblast) velocity [m/s]
u_b	Bulk gas velocity [m/s]
u_c	Coflow velocity [m/s]
u_l	Liquid (fuel or water) jet velocity [m/s]
$\mathcal{W}$	Weighted combination of the segmentation metrics
We	Weber number $\left(We = \frac{\rho_g\, u_b^2\, d_l}{\sigma}\right)$
We_{cr}	Critical Weber number
x	Streamwise (or axial) coordinate [mm]
y	Transverse (or radial) coordinate [mm]
y_b	Axial component of sheet prior to breakup [mm]
ψ	Generic variable (e.g., r_s)
$\overline{\psi}$	Mean of generic variable
ψ'	Fluctuation of generic variable
CV	Computer Vision
DNN	Deep Neural Network
FN	False Negatives
FOV	Field of View
FP	False Positives
FPN	Feature Pyramid Network
GLI	Gas-liquid-interface
GT	Gas Turbine
JiCF	Jet-in-crossflow
LIF	Laser-induced fluorescence
ML	Machine learning
PDF	Probability Density Function
PDI	Phase Doppler Interferometry
PS	Pressure swirl (spray)
TP	True Positives

To measure the intricate breakup dynamics of liquid jets, films, sheets or ligaments, background illumination shadowgraphy is widely employed, allowing for the visualisation of spray processes. Adequate image post-processing can offer a quantitative delineation from primary atomization (Kang et al., 2024), growth of instabilities (Petry et al., 2022) to droplet sizing of spherical and non-spherical droplets and ligaments (Jose and Hampp, 2024) as well as to infer vaporisation rates (Stöhr et al., 2021).

Depending on the measurement campaign, shadowgraphy often yields huge amount of data, necessitating accurate and efficient post-processing methodologies to infer physical insights of the atomization process (Chaussonnet et al., 2018). Conventional algorithm-based computer vision (CV) methods have been used for decades in various disciplines providing a foundation for scientific image analysis. Algorithm-based CV techniques are commonly used for object detection and high- and low-level image processing in various fields, including combustion (Hampp and Lindstedt, 2017; Stöhr et al., 2021), spray analysis (Jose and Hampp, 2024), image enhancement (He et al., 2010) and foundational image processing steps including background subtraction (Kaewtrakulpong and Bowden, 2002; Godbehere et al., 2012). Object detection (Vaithiyanathan et al., 2019) and tracking (Bradski, 1998) can subsequently be conducted through binary image generation and segmentation techniques such as thresholding (Otsu, 1979; Kapur et al., 1985). Many algorithm-based edge detection and segmentation methods have been successfully employed in disciplines like medical imaging (Zhang et al., 2001; Hoover et al., 2000), remote sensing (Pesaresi and Benediktsson, 2001; Li et al., 2010) and autonomous driving (Sotelo et al., 2004; He et al., 2004). The detailed object data gathered through such methods can also be used to create synthetic datasets for training and validating machine learning (ML) models (Jose and Hampp, 2024). Traditional CV methods, while effective, can be computationally expensive and less adaptable to different domain parameters due to varying imaging conditions and require dataset specific parameter tuning. An innate issue in this context is the high sensitivity to aesthetic or structural image features (Szeliski, 2022). Shadowgraphy images are prone to aberrations and intensity fluctuations, e.g., due degrading window quality impeding optical access, light source fluctuations or varying background illumination, which in turn would necessitate project-specific refactoring of the CV algorithm (Schäfer et al., 2020).

Machine learning-based methodologies for CV, particularly deep neural networks (DNNs), are extremely powerful and can offer improved generalisation with equal accuracy in instance or semantic segmentation tasks. This is attributed to the ability of ML models to approximate the mapping function between inputs and outputs. In other words, ML models can learn to predict the correct outputs from the given inputs circumventing the need to hardcode algorithms for each use case. ML models are being used effectively in a plethora of diverse fields such as recommender systems (He et al., 2017), robotics (Kober et al., 2013) and natural language processing (Touvron et al., 2023). Recently, deep learning models, i.e., network architectures with numerous layers or submodules, are being used in complex CV tasks: high-quality image synthesis using denoising diffusion (Ho et al., 2020), real-time object detection (Redmon et al., 2016) and high-quality instance segmentation (He et al., 2020). The large number of tunable parameters, i.e., weights, renders such approaches robust and generalisable. In semantic segmentation, where the model can localise objects of interest with pixel-wise accuracy, the detected masks can be used for highly sensitive CV tasks with utmost accuracy. For scientific purposes, the accurately detected individual object masks can also be used for various statistical data analysis tasks such as edge detection and shape analysis offering a detailed delineation of the involved physical processes.

Recent studies have used segmentation/classification ML models for processing image data from advanced measurement techniques such as laser-induced fluorescence (Hu et al., 2019), light-sheet fluorescent imaging (LSFI) (Packard et al., 2017), hydroxyl LIF (Strässle et al., 2024), shadowgraphy (Jose and Hampp, 2024) and particle image velocimetry (Chun-Yu et al., 2021). Particularly in combustion science, several of these ML-based strategies have been applied to flame and spray analysis. Großkopf et al. (2021) used both instance and semantic segmentation models for detecting industrial burner flames and Pérez-Guerrero et al. (2022) used U-Nets to segment flames for extracting their geometric characteristics for safety analysis. An extension of this methodology to sprays was presented by Huzjan et al. (2023), who used an U-Net model variant to segment fuel sprays with the objective to infer spray cone angle, spray area and penetration depth. Similar approaches have been also applied to agricultural sprays (Acharya et al., 2023). All aforementioned studies used a single configuration and set of domain parameters with their general applicability and transferability to different domains not evaluated.

The current work overcomes such limitations and uses modified semantic segmentation models to accurately analyse three different sprays visualised via shadowgraphy. The first is a pressure-swirl spray, where centrifugal forces form a swirling conical liquid sheet that undergoes atomization into ligaments and fine droplets. This promotes rapid evaporation and mixture homogenisation and is critical for GT combustion. Second, JiCF sprays operate by injecting liquid jets into a gaseous crossflow, where atomization is governed by shear forces at the gas-liquid interface (GLI) driving the growth of instabilities and atomization. Such configurations are prevalent in multi-hole variants for GT combustors, internal combustion engines and agricultural sprays. Third, prefilming airblast atomization utilises high-momentum airflow to destabilise liquid wall films and realise break-up into ligaments and droplets at the airblast edge. This method is widely applied in aero-engine combustion systems. Although shadowgraphy is the common technique used, the images from each of these measurement campaigns vary aesthetically in their intensity levels, dynamic range, signal-to-noise ratio and spatial resolution. Apart from the aesthetic features, they also significantly vary structurally due to the different types of injectors and therefore atomization mechanism used. Moreover, the operation conditions, i.e., Reynolds and Weber numbers, fluid flow rates and air preheat temperature, as well as physical liquid properties, i.e., water and kerosene, vary in the present study. While this renders systematic comparison between the different sprays difficult, it serves the present purpose of developing a general applicable and transferable ML-based spray detection model. The developed ML-based methods ought to substitute conventional algorithm-based image binarisation processing steps. The main objectives are highly accurate masks, transferability across datasets and reducing inference (i.e., post-processing) time to analyse spray shadowgraphy images from varying experimental setups and quality. Section 2 describes the three experimental configurations used and Section 3 describes the ML models, training approach and statistical data analysis. The final ML model, trained solely on jet-in-crossflow sprays, is subsequently applied to segregate JiCF, hollow cone pressure swirl spray and a prefilming airblast spray in Section 4. The results show that the model is capable for semantically segmenting sprays from all three measurement campaigns. Subsequently, the resulting masks create the foundation for a statistical analysis on the involved turbulence-spray interactions, such as gas-liquid-interface disturbance amplitudes and curvature.

2. Experimental configuration

For all three injectors, the same base canonical flow spray channel, depicted in Fig. 1 and described in detail by Schäfer et al. (2020), has been used for the current investigation. The apparatus consists of a main air intake, a contraction nozzle equipped with flow straightening elements and an optically accessible measurement section confined by quartz glass windows. The optical section has a cross-section of $40 \times 40\,\mathrm{mm}^2$ and a length of 400 mm. For the PS sprays, a separately controlled wall air film generator is positioned between the contraction nozzle and the optical section to create a protective coaxial air shield for the inner quartz glass surface. This reduces surface wetting and improves the optical access for prolonged measurement time. The horizontal end of the wall is located 1.0 mm upstream of the atomizer tip. It is worth mentioning, that the wall air film does not influence the primary break-up that is the focus of the present study (Schäfer et al., 2020). Pressurised Howden air is supplied, and the flow rate is regulated by a mass flow controller (Bronkhorst EL-Flow series). A PID controlled air preheating system with 38 kW electrical power can be utilised for preheating the air flow. The liquid is supplied by a nitrogen pressurised stainless steel piston cylinder with the flow rate controlled via a liquid mass flow controller (Bronkhorst mini CORI-FLOW M14) and guided into the supply system. Downstream of the test section, the droplet-laden flow is cooled, and the dispersed phase separated by means of a wire mesh demister. This infrastructure is used for all three setups unless specified otherwise.

2.1. Key dimensionless parameters

Prior to describing the specific spray setups, the following parameters are defined that characterise the flow and spray breakup across various operating conditions. The term liquid is used here for the utilised working fluids of fuel or water and the term gas is used for air. The liquid jet velocity u_l is defined by

$$u_l = \frac{4\,\dot{m}_l}{\pi\, d_l^2\, \rho_l}, \qquad (1)$$

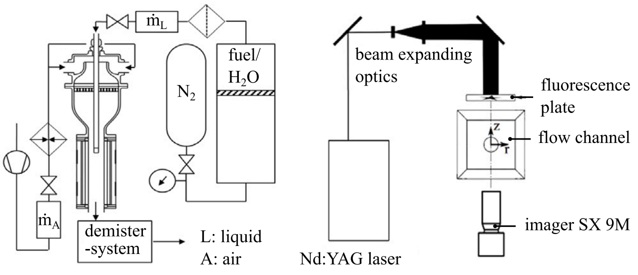

Fig. 1. Schematic representation of the experimental configuration and the optical diagnostic setup (shadowgraphy).

where $\dot{m}_l$ is the liquid mass flow rate, d_l is the nozzle diameter, and ρ_l is the liquid density. The momentum flux ratio q is given by

$$q = \frac{\rho_l\, u_l^2}{\rho_g\, u_b^2}, \tag{2}$$

where ρ_g is the gas density and u_b is the bulk gas velocity. The Weber number We is expressed as

$$We = \frac{\rho_g\, u_b^2\, d_l}{\sigma}, \tag{3}$$

where d_l the injector orifice diameter and σ is the liquid surface tension. The gas-phase Reynolds number Re_g is defined by

$$Re_g = \frac{\rho_g\, u_b\, d_h}{\mu_g}, \tag{4}$$

where μ_g is the dynamic viscosity of the gas and d_h the hydraulic channel diameter. The liquid jet Reynolds number Re_l is given by

$$Re_l = \frac{\rho_l\, u_l\, d_l}{\mu_l}, \tag{5}$$

where μ_l is the dynamic viscosity of the liquid. Finally the mass flow rate ratio α is defined by

$$\alpha = \frac{\dot{m}_l}{\rho_g\, A\, u_b}, \tag{6}$$

where A is the area of cross section of the flow channel.

2.2. *Pressure swirl spray*

The first spray configuration investigates a hollow cone pressure swirl spray. In the current study, a commercial Schlick V121 atomizer with an orifice diameter of 0.15 mm and nominal spray angles of 60° is mounted onto the tip of the central working fluid supply lance, as shown in Fig. 2. The working fluid supply lance is water cooled to maintain the temperature and thus physical properties constant regardless of the operation condition variations. Three different air coflow conditions (u_b) are investigated, while maintaining the liquid mass flow rate ($\dot{m}_l$) constant as specified in Table 1. Deionised water is used as the working fluid for the PS investigations.

2.3. *Jet-in-crossflow spray*

The same test rig as for the PS investigation is used for the JiCF spray with three adjustments, see Fig. 3. First, one quartz glass wall is replaced by a metal plate through which the single plain orifice injector is inserted. This also allows to remove the centralised fuel supply lance (i.e., the second alternation). The wall air film nozzle is removed (third adjustment) to inject the liquid jet directly into a well defined crossflow. The tip of the single plain orifice injector aligns with the inner wall surface and exhibit an orifice diameter of 200 μm and length to diameter ratio of 10. The injection occurs in a 90° angle to the crossflow. The working fluid for the JiCF spray is kerosene (i.e., Jet A-1) at a liquid temperature of 293 K and the air preheat temperature is set to 473 K using a PID controlled inline heater. Otherwise, the identical flow controller setup and liquid fuel supply system of the PS study is utilised here. A full matrix of the test conditions is provided in Table 2.

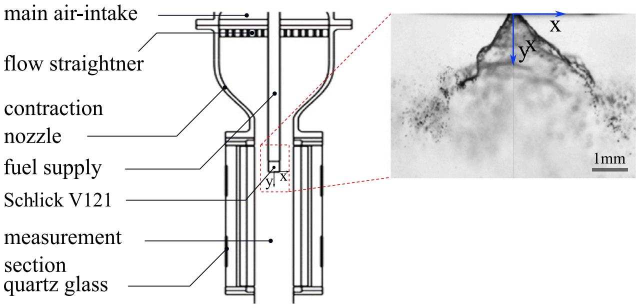

Fig. 2. Schematic representation of the spray channel used for the pressure swirl spray and the corresponding image obtained from shadowgraphy. The air flow and the liquid spray is injection from the top towards the bottom. The coordinate system for this spray configuration is also introduced.

Table 1
Conditions for air coflow and Schlick injection, where u_b and $\overline{u_w}$ are bulk coflow and wall film velocity, We_{cr} the coflow Weber number, T_g and T_w the air and wall film temperatures respectively, $\dot{m}_l$ the water mass flow rate, q is the momentum flux ratio, α is the mass flow rate ratio, ΔP_l the pressure drop across the injector and Re_g, the coflow Reynolds number.

prop.	Unit	S1 W	S2 W	S3 W
Air coflow conditions				
u_b	m/s	20	35	50
T_g	K	298	298	298
Re_g	$\times 10^4$	5.1	8.9	12.7
$\overline{u_w}$	m/s	19.5	34.4	48.9
T_w	K	473	473	473
q	–	1342	438	215
α	$\times 10^{-1}$	0.11	0.06	0.4
Schlick injection conditions				
We	–	1.0	3.0	6.1
We_{cr}	–	8.8	0.3	18
$\dot{m}_l$	g/s	0.40		
ΔP_l	bar	10.0		

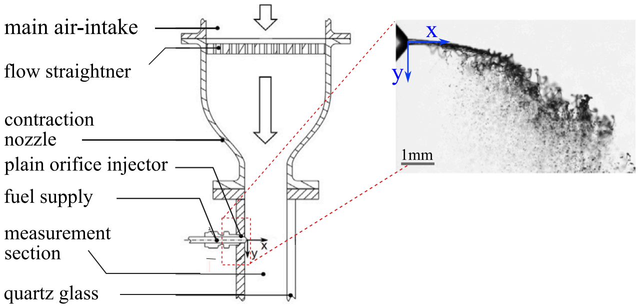

Fig. 3. Schematic representation of the spray channel used for the jet-in-crossflow spray and the corresponding image obtained from shadowgraphy. The air flow is from the top to the bottom, while the fuel jet is illustrated in shadowgraphy image. The coordinate system for this spray configuration is also introduced.

2.4. *Prefilming airblast atomization spray*

The third type of spray investigated is a prefilming airblast spray. In the present canonical experiment, the entire air inflow section is replaced by a manifold that allows splitting the air flow into coflow and atomization air stream, see Fig. 4, both regulated by two independent mass flow controllers. The optical test section is identical to the PS study, yet the air wall film duct is also removed. The coflow and atomization air streams are separated by a flat and polished wall with

Table 2
Conditions for air crossflow and fuel jet injection, where u_b and $\dot{m}_l$ are air crossflow velocity and liquid fuel mass flow rate, respectively. q is the momentum flux ratio, α is the mass flow rate ratio, We is the Weber number and, Re_g and Re_l are the gas and fuel jet Reynolds numbers respectively.

Case	u_b (m/s)	$\dot{m}_l$ (g/s)	q –	α $\times 10^{-1}$	We –	Re_g $\times 10^5$	Re_l $\times 10^3$
JiCF1J	65	0.5	100	0.06	28	1.0	2.2
JiCF2J	65	1.0	399	0.13	28	1.0	4.3
JiCF3J	65	2.0	1595	0.26	28	1.0	8.7
JiCF4J	99	0.5	43	0.04	64	1.6	2.2
JiCF5J	99	1.0	172	0.08	64	1.6	4.3
JiCF6J	99	2.0	688	0.17	64	1.6	8.7
JiCF7J	133	0.5	24	0.03	115	2.1	2.2
JiCF8J	133	1.0	95	0.06	115	2.1	4.3
JiCF9J	133	2.0	381	0.12	115	2.1	8.7

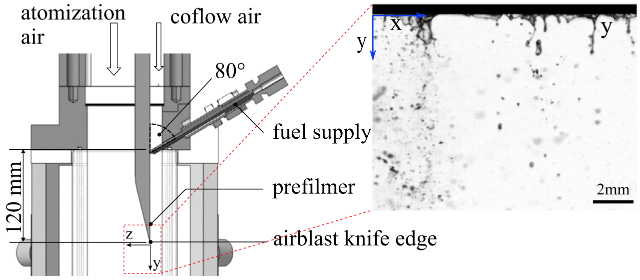

Fig. 4. Schematic representation of the spray channel used for the prefilming airblast spray and the corresponding image (side view) obtained from shadowgraphy. The coflow and airblast air stream, as well as the fuel wall film flow from the top towards the bottom. The coordinate system for this spray configuration is also introduced. The top edge of the shadowgraph includes the bottom edge of the prefilmer followed by the dispersed spray.

an airblast knife edge. The wall separates the optical test section into two rectangular ducts with cross-sections of 40 × 10.5 mm^2 on the prefilming and coflow side and 40 × 26.5 mm^2 on the atomization air side. The wall length from the injection point to the airblast edge is 120 mm with a thickness of 3 mm. The wall is thickened at the side walls to 8 mm to allow for sealing against the adjoining quartz glass windows to avoid fluid exchange upstream of the airblast knife edge. Here, the two ducts merge into the original channel with 40 × 40 mm^2 cross-section.

Prefilming is conducted by means of three 100 µm plain orifice jet-in-crossflow injectors that are supplied from a common fuel plenum with the kerosene (Jet A-1) mass flow regulated by same flow controller setup described above. In the current study, the injection angle is maintained at 80°, yet can be also set to 20° and 50°. The rest of the fuel supply system is identical to the ones described above. The JiCF prefilming sprays are directed towards the wall, where a thin film is created, spread out and convected downstream to the airblast edge by the coflow air velocity (u_c). The shear between the airblast air velocity (u_a) and u_c across the airblast edge leads to atomization of the thin film. In the current study, the ratio of u_a and u_c is varied along with the fuel mass flow rate ($\dot{m}_l$) as listed in Table 3. The coflow and airblast air, fuel and wall temperature are maintained at 293 K.

2.5. Shadowgraphy

Quantitative spray atomization analysis is conducted on the basis of background illumination shadowgraphy as illustrated in Fig. 1 (right). The second harmonic of a Nd:YAG Spectra Physics Quanta Ray laser pulse pair (repetition rate 10 Hz, Δt = 10 µs) is directed onto a fluorescent screen. In the current work only the first laser pulse is used, yet the double pulse would facilitate droplet velocimetry.

Table 3
Conditions for air coflow and prefilming airblast injection, where u_c and u_a are coflow and atomization air velocities, $\dot{m}_l$ is the liquid fuel mass flow rate, Θ is the spray angle, α is the mass flow rate ratio, $Re_{g,c}$ is the Reynolds number for the coflow air, and $Re_{g,a}$ is the Reynolds number for the airblast air.

Case	u_c (m/s)	u_a (m/s)	$\dot{m}_l$ (g/s)	Θ (°)	$Re_{g,c}$ $\times 10^3$	$Re_{g,a}$ $\times 10^3$	α $\times 10^{-2}$
A1J	80	80	0.40	80	86	164	0.13
A2J	80	40	0.40	80	86	82	0.17
A3J	80	60	0.40	80	86	123	0.15
A4J	40	80	0.40	80	43	164	0.17
A5J	60	80	0.40	80	64	164	0.15
A6J	100	80	0.40	80	107	164	0.11
A7J	120	80	0.40	80	129	164	0.10
A8J	120	20	0.40	80	129	41	0.15
A9J	80	80	0.20	80	86	164	0.06
A10J	40	80	0.20	80	43	164	0.09
A11J	120	80	0.20	80	129	164	0.05
A12J	80	80	0.60	80	86	164	0.19
A13J	40	80	0.60	80	43	164	0.26
A14J	80	80	0.80	80	86	164	0.26
A15J	40	80	0.80	80	43	164	0.03

Upon excitation at 532 nm, the fluorescent screen produces the desired non-coherent red-shifted background illumination (Stöhr et al., 2021; Schäfer et al., 2020) with peak emission at 655 nm (FHWM = 65 nm). The fluorescence decay time, and therefore the image exposure time, is determined to ∼20 ns. The laser pulse energy has been adjusted between the different experimental setups to result in an optimum dynamic range utilisation (e.g., 3000–3500 counts) of the utilised CCD camera (LaVision Imager SX 9M, double frame, 12 bit, 3360 × 2712 pixels^2, minimum shutter time of 42 µs), while avoiding over-exposure.

To record the shadowgraphy images, the camera is synchronised with the laser by a programmable timing unit (LaVision PTU-X). The quantum efficiency of the camera chip (Sony ICX 814) in the wavelength range of the background illumination is 55 ±10%. The internal camera gain to electronically amplify the signal is set to the minimum of 0.0 dB (the default value) to minimise noise. The camera is equipped with a Nikon macro lens with a focal length of 200 mm and the f-number is set to f/2.8. For the JiCF, PS and airblast spray the field of views (FOV) are $13.0 \times 10.5\,\text{mm}^2$, $27.9 \times 18.3\,\text{mm}^2$ and $13.1 \times 10.1\,\text{mm}^2$, resulting in optical resolutions (measured via a USAF 1951 resolution target) of approximately 12.4 µm, 26.4 µm and 12.9 µm in the focal plane, respectively. As shadowgraphy is a line-of-sight integrating measurement technique, out-of-plane objects are also recorded, yet with degrading optical resolution. In the primary breakup region, i.e., the focus of the current study, the measured signal-to-noise ratios (SNR) of the JiCF, PS and airblast sprays are 16, 7.6 and 14, respectively.

3. Methodology

In order to delineate the effect of aerodynamic forces on primary atomization and to provide a quantitative description of the involved interactions, precise and accurate segmentation of the sprays from the surrounding gaseous phase (i.e., background in the shadowgraphy images) is essential. Subsequently, characteristics such as spray angle, disturbance amplitudes, break-up length and curvature can be inferred from the segmented gas-liquid-interface (GLI) contours.

3.1. ML-based method for spray segmentation

ML models are implemented to generalise the segmentation of spray with varying domain parameters. The approach involves generating training data and model evaluation. Focus is also given to reduce annotation effort through automatic labelling. Following this, a comprehensive statistical analysis is conducted with the ML-augmented data analysis framework to evaluate the generalisability and robustness of the selected model.

Table 4

Model comparison. SF: Semantic FPN, DL: DeepLabV3+, D1: Dataset made from a single preliminary JiCF case (JiCF0J: $u_b = 64\,\mathrm{m/s}$, $\dot{m}_l = 0.5\,\mathrm{g/s}$; liquid: Jet A-1), D2: Dataset made from multiple JiCF spray cases (JiCF0J-JiCF9J: $u_b = 64\,\mathrm{m/s}$, $65\,\mathrm{m/s}$, $99\,\mathrm{m/s}$ and $133\,\mathrm{m/s}$; $\dot{m}_l = 0.5\,\mathrm{g/s}$, $1.0\,\mathrm{g/s}$, $2.0\,\mathrm{g/s}$; liquid: Jet A-1).

ML model	1	2	3	4	5
Base model	SF	SF	SF	SF	DL
Augmentation (Geometric)	N	N	Y	N	N
Augmentation (Aesthetic)	N	N	N	Y	N
Dataset used	D1	D2	D2	D2	D2

3.1.1. Training data generation

The training data for the ML models are generated from the experimental raw JiCF spray data due to its aesthetic quality and high signal-to-noise ratio. These images with spatial dimensions of 3260 $\times$ 2712 pixels^2 are then normalised between 0 and 255 and resized to 1024 $\times$ 851 pixels^2 by pixel binning considering memory constraints and to preserve the original aspect ratio. Subsequently, the generated datasets have a total of 1500 greyscale images each accompanied by the corresponding annotations (ground truths). The following steps are adopted to generate the training data.

- From the input raw image, the corresponding ground truth mask is generated using supervised conventional segmentation methods resulting in a binary image, where the background regions are represented by zeros and spray regions are represented by ones (Jose and Hampp, 2024).
- Augmentations, if any, are applied randomly to both input and ground truth images.
- The input–output pair and the corresponding metadata are saved to a data file for the model training.
- The above steps are iterated over different input images forming a complete dataset.
- The dataset is split into training, testing, and validation sets in the ratios 0.6, 0.3 and 0.1, respectively.

The models are trained using two distinct datasets to optimise performance. The first dataset (D1) consisted of raw images obtained from a single jet-in-crossflow spray configuration and operation condition, serving as the primary data source. To further enhance the model's generalisation capability, a second dataset (D2) is developed, incorporating images of JiCF sprays across multiple operation conditions at varying momentum flux ratio and Reynolds numbers. It is worth highlighting that the training data consist solely of JiCF sprays and the models have not seen any PS or airblast sprays in the training process. Generating high-quality ground-truth annotations is often challenging (Urbán et al., 2020), primarily because image features — such as noise, camera artefacts, local intensity fluctuations, and focus irregularities — can substantially affect segmentation algorithms. In an effort to streamline the annotation process, we adopt a strategy in which only the most pristine images (spray cases) are annotated, thereby allowing conventional segmentation methods to perform reliably. To ensure realism and robust performance in broader contexts, these idealised images are then augmented synthetically with the aforementioned image features as outlined in Table 4. This approach preserves annotation accuracy while introducing a variety of real-world perturbations that enhance the robustness and generalisability of the resulting segmentation models. The validation dataset is however, replaced by a new set of annotated validation data that consists of all three spray conditions to provide a more meaningful evaluation of the trained models. See also Section 4.1.

3.1.2. Augmentations

Machine or deep learning is associated with large datasets to facilitate their comprehension of complex features, better generalisation, reduced over-fitting, higher prediction accuracy and robustness (Halevy et al., 2009; Sun et al., 2017). The significance lies in proper sampling of the data reducing class imbalance with appropriate representation of the population. Data augmentations can be used to synthetically enlarge existing datasets and overcome class imbalances and missing data. Such steps improve feature learning and model generalisation, thereby enhancing predictions in real world scenarios (Krizhevsky et al., 2012). In this work, foundational geometric augmentations such as cropping and flipping are combined with aesthetic augmentations including random brightness and contrast adjustments.

3.1.3. Model selection, training, and evaluation

A thorough investigation of various ML based image segmentation techniques is conducted. The specific structure of the sprays enables the use of semantic segmentation models in contrast to instance or panoptic segmentation models that can necessitate higher model complexity and computational effort. Two state-of-the-art model architectures (i.e., Semantic FPN and DeepLabV3+) are compared in the current study.

3.1.4. Semantic FPN

Semantic FPN (Kirillov et al., 2019) extends the structure of Feature Pyramid Network (FPN) (Lin et al., 2017) with a lightweight semantic head that produces corresponding segmentations. The general FPN contains two pathways, a bottom up pathway, that downsamples the input image progressively producing a pyramid like structure. The second one, i.e., top-down pathway, takes the output of the bottom-up pathway (high-level semantic feature maps) and applies progressive upsampling while combining them with the corresponding high-resolution feature maps from the bottom-up pathway through lateral connections. In contrast to the top-down pathway of the FPN, in Semantic FPN the multiscale feature maps of the pathway are convoluted, upsampled and then summed to produce a unified segmentation map. This architecture increases the efficiency and robustness of the model by reducing model complexity and incorporating multiscale features with further details provided in the supplementary methods and materials (SMM).

3.1.5. DeepLabV3+

DeepLabV3+ (Chen et al., 2018) builds on the popular foundational DeepLab model (Chen et al., 2017a) and later versions (Chen et al., 2017b) enhancing the performance with depth-wise separable convolutions and an encoder–decoder structure. Former DeepLab models were characterised by mainly atrous convolutions and atrous spatial pyramid pooling. In contrast to normal convolutions, in atrous convolutions certain parts of the kernel are zeroed out. This allows to incorporate a wider field of view without sacrificing the computational efficiency. Thus, denser features can be accumulated in the feature maps with the same parameters as normal convolutions. In the model backbone, these atrous convolutions are applied in place of conventional kernels. In order to account for multiscale features spatial pyramid pooling is used. Here, output feature maps from atrous convolutions with varying kernel rates are combined into a single feature map. In the final DeepLabV3+ model, instead of using standard convolutions, first a depth-wise atrous convolution is applied followed by a pointwise convolution, thereby reducing the computational complexity. The new architecture uses DeepLabV3 as the encoder producing input feature maps for the decoder, which upsamples the input feature maps to produce segmentation maps with further details provided in the SMM.

3.1.6. Training approach

To achieve the maximum performance and faster convergence, transfer learning is applied to both architectures. Pre-trained weights trained on ImageNet (Deng et al., 2009) and Cityscapes (Cordts et al., 2016) are used as initiators. The model backbones are frozen during the transfer training. Apart from the most default configurations from the models' literature, hyper-parameters like learning rate (0.00025), batch size (16) and momentum (0.9) are kept the same for both models for consistency. Both models are trained for a maximum of 80,000 iterations. To refine masks and thereby enhance the segmentation accuracy, both models are supplemented by PointRend (Kirillov et al., 2020). The latter performs pixel-based selective segmentation inferences adapting to increased segmentation effort for high-quality object boundaries. This addition significantly improves the models' ability to capture fine details and complex shapes, as often present in scientific images, where precise segmentation is crucial.

3.1.7. Evaluation metrics

Training performance and model stability is inferred from the loss curves. Periodic validations are carried out using an external dataset consistent of all three sprays to provide meaningful segmentation metrics explained below. The choice of the evaluation metrics is important considering the diverse parameters and augmentations used in the study (see Table 4). Intersection over Union or Jaccard index ($\mathcal{J}$) measures the average overlap between the predicted segmentation mask and ground truth. Considering the necessity for accurate spray segmentation, the Jaccard index of the spray class ($\mathcal{J}_1$) is considered a significant metric. It is defined as:

$$\mathcal{J}_1 = \frac{\mathrm{TP}_1}{\mathrm{TP}_1 + \mathrm{FP}_1 + \mathrm{FN}_1}, \tag{7}$$

where TP_1, FP_1, and FN_1 denotes pixel-wise True Positives, False Positives and False Negatives for the spray class respectively. To provide an overall measure of segmentation performance across both the spray class and the background, the mean Jaccard index, ($\overline{\mathcal{J}}$) is calculated as:

$$\overline{\mathcal{J}} = \frac{1}{k} \sum_{i=0}^{k-1} \mathcal{J}_i, \tag{8}$$

where k is the number of classes. Since boundary accuracy is critical for extracting precise spray contours, the boundary Jaccard index for the spray class ($\mathcal{J}_{\mathrm{B},1}$) is also considered.

$$\mathcal{J}_{\mathrm{B},1} = \frac{\mathrm{TP}_{\mathrm{B},1}}{\mathrm{TP}_{\mathrm{B},1} + \mathrm{FP}_{\mathrm{B},1} + \mathrm{FN}_{\mathrm{B},1}}, \tag{9}$$

$\mathrm{TP}_{\mathrm{B},1}$, $\mathrm{FP}_{\mathrm{B},1}$, and $\mathrm{FN}_{\mathrm{B},1}$ represent the True Positives, False Positives, and False Negatives along the boundary of the spray class, respectively. All the above-mentioned metrics are similarity scores between the ground truth and predictions, where zero indicates no overlap and one indicates perfect overlap. Additionally, the pixel accuracy for the target class, $\mathcal{A}_1$, i.e., the fraction of correctly classified target class pixels, is defined as:

$$\mathcal{A}_1 = \frac{\mathrm{TP}_1}{\mathrm{TP}_1 + \mathrm{FN}_1}. \tag{10}$$

Finally, these metrics are combined into a single weighted mean ($\mathcal{W}$):

$$\mathcal{W} = w_1 \cdot \mathcal{J}_1 + w_2 \cdot \overline{\mathcal{J}} + w_3 \cdot \mathcal{J}_{\mathrm{B},1} + w_4 \cdot \mathcal{A}_1, \tag{11}$$

where $w_1 = 0.5$, $w_2 = 0.20$, $w_3 = 0.15$ and $w_4 = 0.15$. These weights reflect the relative importance of each metric in the overall evaluation, with higher weights assigned to metrics that are more critical for the specific segmentation task. To emphasise accurate spray segmentation, the largest weight ($w_1 = 0.5$) is assigned to the Jaccard index of the spray class $\mathcal{J}_1$. Since the background class can dominate overall performance metrics, a high weight on $\mathcal{J}_1$ ensures the spray region itself is captured effectively. Meanwhile, the mean Jaccard index $\overline{\mathcal{J}}$ gauges the model's consistency across both spray and background classes, and the boundary Jaccard index $\mathcal{J}_{\mathrm{B},1}$ and pixel accuracy $\mathcal{A}_1$ are included to ensure precise boundary delineation and robust pixel-level classification, both of which are crucial for accurate GLI detection.

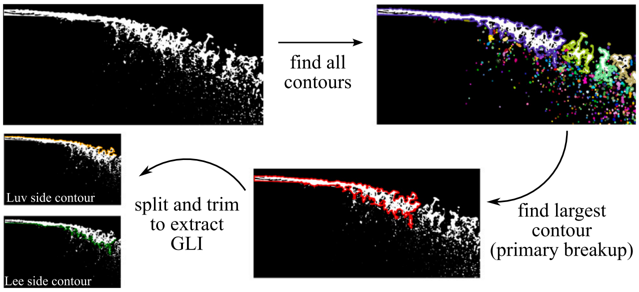

Fig. 5. Illustration of the contour extraction process for the binarised images produced by the ML-model.

3.2. Active filtering

While the model accurately segments vast majority of sprays, domain artefacts (like uncut spray contours) are visible in the inferences of a low number (2%–4%) of PS sprays. This is not related to any specific spray structure but rather arises due to parameter tuning limitations within our data-analysis framework during post processing of the binarised images generated by the ML-model. Considering that enough number of images are available for the current statistical analysis, these images are considered as outliers and are omitted using active filtering during post-processing. This ensures the consistency and reliability of the data.

3.3. Statistical analysis

For the subsequent statistical analysis of the spray atomization characteristics, first an accurate contour of the gas-liquid-interface based on the binarised images obtained from the ML-model is extracted as depicted in Fig. 5. It involves the following steps:

- A general contour extraction algorithm is run on the binarised image followed by eliminating all the contours except the largest one, which represents the spray contour until primary breakup.
- For both JiCF and PS sprays, the single contour enclosing the spray is split into two segments. Specifically, for the JiCF into 'lee' (leeward side - sheltered from the incoming gas flow) and 'luv' (windward side - facing the incoming gas flow) side of the injector and for the PS into left and right spray cone sheet.
- The contours are trimmed to avoid overlapping and irregularities.

- The instantaneous contours are used for GLI statistical calculations.

For every spray characteristic (ψ) and N number of instantaneous sheets (or images), the mean and standard deviation are calculated based on Eqs. (12) and (13), respectively.

$$\bar{\psi} = \frac{1}{N} \sum_{n=1}^{N} \psi_n \tag{12}$$

$$(\psi' \psi') = \frac{1}{N} \sum_{n=1}^{N} (\psi_n - \bar{\psi})^2 \tag{13}$$

3.3.1. Breakup length calculation

For each instantaneous PS sheet, the breakup length is calculated based on the Euclidean norm of the trailing sheet position, i.e., $l_\mathrm{b} = (r_\mathrm{b}^2 + y_\mathrm{b}^2)^{1/2}$ to facilitate a comparison with Petry et al. (2022). For the JiCF sprays, the contour curvature is considered and the breakup length is calculated by the cumulative sum of the Euclidean distances between consecutive boundary points, i.e., the length of the unrolled spline (l_s). The latter approach inherently includes jet bending effects and

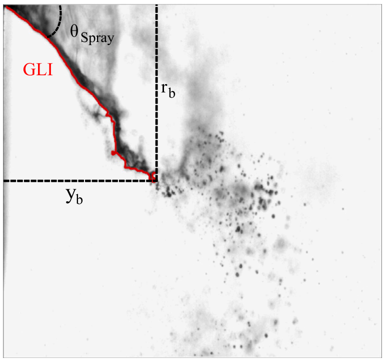

Fig. 6. Schematic showing the 90° rotated PS spray and the detected spray contour (GLI) with its axial and radial components. The image has been rotated solely for data analysis purposes to analyse all sprays from left to right. Subsequent results are transformed back into the original coordinate system defined in Fig. 2.

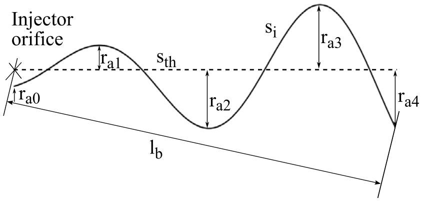

Fig. 7. Schematic showing the calculation of disturbance amplitudes.

is thus preferred for JiCF sprays. For completion, the breakup length in jet injection (l_x) and crossflow direction (l_y) is also determined. Subsequently, the mean breakup length ($\bar{l}$) and its fluctuation (l') are calculated.

3.3.2. Spray angle

The PS half spray cone angles for each instantaneous sheet is calculated using the axial and radial components of the trailing edge position of the instantaneous sheet (i.e., $\theta_s = 180/\pi \cdot \arctan(\frac{r_b}{y_b})$) as illustrated in Fig. 6. Since the current analysis focuses on the primary break-up mechanism, the influence of turbulence on spray angle calculations is minimised by considering only the linear segment of the spray sheet, before any bending or wrinkling occurs. Thus, differences in the spray angle can be attributed, in part, to differences in the static pressure at the injector orifice (Moon et al., 2009). Considering the detected modest axial asymmetry of the Schlick sprays, the full cone angle is obtained by, $\Theta_s = \theta_{s,left} + \theta_{s,right}$. Subsequently, the mean and standard deviation of the spray angles are calculated over all instantaneous images and detections using Eqs. (12) and (13).

3.3.3. Gas-liquid-interface fluctuations

The bounding iso-contour of the spray sheet or jet is exposed to high momentum turbulent air flow. This leads to corresponding turbulent fluctuations of the GLI, quantified by the radial distance (r_s) between the instantaneous GLI contour (s_i) and the notional spray symmetry axis passing through the injector orifice. Further its mean ($\overline{r_s}$ via Eq. (12)), standard deviation (r'_s via Eq. (13)) are calculated. The spatial distribution of s_i can also be referred to as turbulent spray brush and r'_s is consequently its fluctuation width. The extent of turbulent fluctuations is inherently dependent on the aerodynamic forces and the liquid sheet or jet stability. To quantify this, for the JiCF spray, r'_s is binned into segments of 2.0 mm width, up to 10.0 mm away from the injector orifice in the jet direction (x). For the pressure swirl spray the bin width is reduced to 0.5 mm up to an axial distance (y) of 2.0 mm. Subsequently, the distribution of the radial fluctuations (PDF(r'_s)) in each bin is evaluated. The PDF spread illustrates the spatial GLI fluctuation and thus stability towards aerodynamic forces.

3.3.4. GLI curvature statistics

Turbulent fluctuations on the gas–liquid-interface (GLI) can also be characterised by the local curvature, κ. In a two-dimensional image plane, κ at any point on the GLI contour is formally given by,

$$\kappa = \frac{d^2x\,dy - dx\,d^2y}{\left[(dx)^2 + (dy)^2\right]^{\frac{3}{2}}}, \tag{14}$$

where x and y denote the coordinates of the GLI contour along with their derivatives.

In our implementation, the contour points $\{(x_n, y_n)\}$ are first smoothed using a filter (e.g., Savitzky–Golay) to reduce noise. Subsequently, the mean and standard deviation of the curvature are calculated over all instantaneous images and detections using Eqs. (12) and (13).

3.3.5. Disturbance amplitude

To quantify the intricate interactions between gas phase turbulence and the spray sheet or jet, the growth of disturbance amplitudes (e.g., Kelvin–Helmholtz) on the gas-liquid-interface are delineated. While r'_s includes bulk motions of the continuous liquid sheet or jet, r_a is the disturbance amplitude defined as the absolute distance of an instantaneous GLI contour (s_i) peak to a theoretically undisturbed sheet or jet (s_{th}), as illustrated in Fig. 7. To robustly define s_{th}, a regression model with high-order polynomial fitting to identify spurious disturbance peak points is applied, following the method established by Petry et al. (2022). The amplitude between the injector orifice and the first zero crossing (r_{a0}) is omitted due to its negligibly small values and the low signal-to-noise ratio near the nozzle exit. Absolute r_a are categorised into a predefined bins based on their axial distance from the injector orifice. The mean disturbance ($\overline{r_a}$) and its fluctuation (r'_a) in each bin are calculated using the Eqs. (12) and (13), respectively.

3.3.6. Atomization characterisation in prefilming airblast sprays

Prefilming airblast sprays operate by using a high-speed airflow to atomize a liquid film into ligaments and fine droplets. Subsequent to the spray detection via the ML-models, the methodology of Chaussonnet et al. (2018) is applied to analyse the atomization process. For this purpose, the following steps are adopted:

- A precise and closed contour of the liquid film detached from the airblast wall and penetrating into the high shear air flow is obtained defining the gas-liquid-interface. Disconnected ligaments or droplets are excluded from the present analysis.
- As the contour also includes part of the edge of the airblast prefilmer wall, images are cropped to only include the detached liquid film regions. This is indicated by the red line in Fig. 8.
- The complete contour is then divided into segments of 0.3 mm width resulting in 40 bins along the airblast knife edge direction (x), see coloured segments in Fig. 8.
- For each instantaneous image, the minimum (l_{min}) and maximum value (l_{max}) for the liquid film penetration as well as their arithmetic mean ($\bar{l}$) are determined as labelled in Fig. 8. The detached liquid film area in each bin is also calculated.
- Subsequently, the mean and standard deviation of these properties is calculated using Eqs. (12) and (13).

4. Results and discussion

In the following, first the ML-based semantic segmentation models are evaluated in Section 4.1 and subsequently applied to the three types of spray to delineate the interaction between the liquid jets (Section 4.2), sheets (Section 4.3) or films (Section 4.4) with the high momentum air flow.

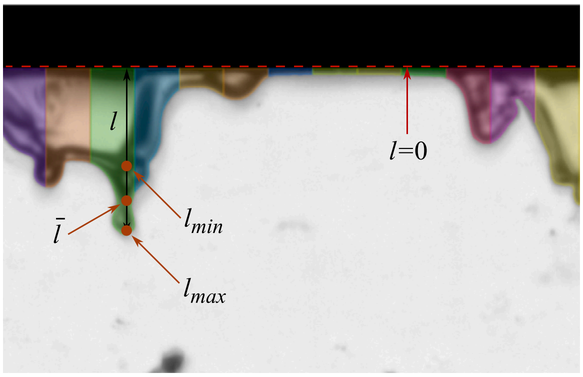

Fig. 8. Illustration of the quantities extracted from each image, where l_{max}, l_{min} and $\bar{l}$ represent the maximum, minimum, and average penetration of the detached liquid film in each bin. The red line shows the airblast wall edge.

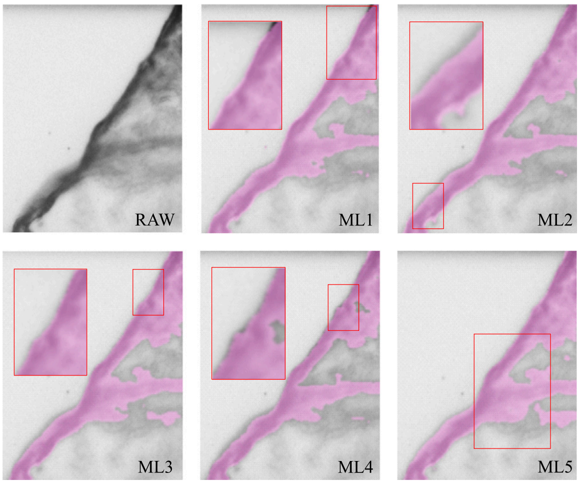

Fig. 9. The illustrated images show model predictions on never-seen data. Minute, yet for the present analysis significant, differences can be observed on the detected masks. For instance, ML1 and ML4 fail to identify certain spray features, while ML2 and ML5 overestimate coverage by including out-of-focus regions. Conversely, ML3 exhibits predictions that closely align with the ground truth.

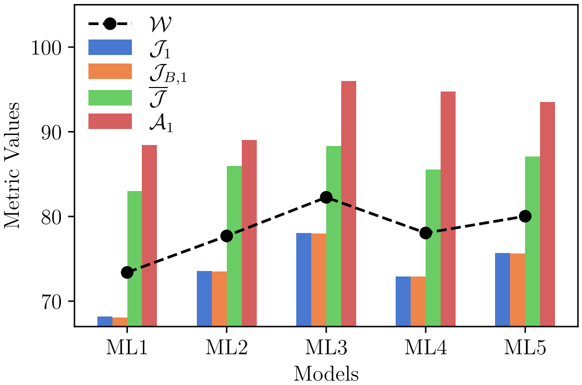

Fig. 10. Segmentation metrics of the tested models. $\mathcal{J}_1$ is the Jaccard index of the spray class, $\overline{\mathcal{J}}$ is the mean Jaccard index, $\mathcal{J}_{B,1}$ is the boundary Jaccard index of the spray class, $\mathcal{A}_1$ is the pixel accuracy of the spray class, and $\mathcal{W}$ is the weighted mean score (see Eqs. (7)–(11)). The metrics identifies ML3 as the best performing model.

4.1. Model evaluation

For model evaluation, a dataset comprised of diverse sprays is curated manually. For this purpose, first spray masks are generated using conventional CV methods. A random sample of the most accurate masks from all three spray types is collected and annotated to create the validation dataset. The latter is used for periodic evaluation against the metrics outlined in Section 3.1.7 and the best performing model is selected based on $\mathcal{W}$ as defined in Eq. (11). As inferred from Fig. 9, ML3 performs the best in terms of mask quality. ML1 and ML4 tend to overfit and produce porous or incomplete masks. In contrast, ML2 and ML5 tend to predict broadened masks and increasingly include background, out-of-plane structures or droplets. The differences between the models are subtle, but are highly relevant for the subsequent contour-based statistical analysis. These observations are further assured and quantified in Fig. 10, where the validation metrics mentioned in Section 3.1.7 are compared for all the models. The metrics as well as the observations on the predicted masks render ML3 the most suitable model for the present purpose. Therefore, ML3 is used for the detailed investigations on turbulence-spray interaction and primary spray atomization.

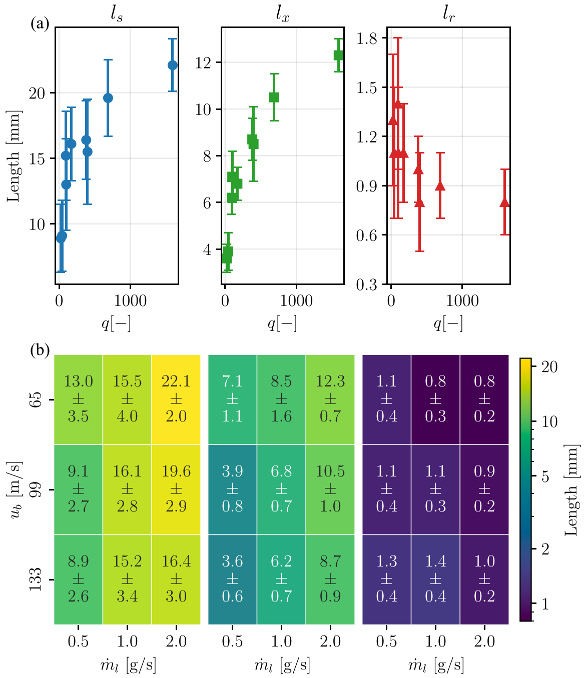

Fig. 11. Scatter plot (a) showing the primary breakup length (l_s) as well as the axial (l_x) and radial (l_r) fuel jet penetration depth as well as their standard deviations for different values momentum flux ratio (q). The heatmap (b) shows the same but for different values of air crossflow velocity (u_b) and fuel mass flow rate ($\dot{m}_l$).

4.2. Jet-in-crossflow (JiCF) spray

Nine different JiCF sprays with varying momentum flux ratio, i.e., air crossflow velocity (u_b) and fuel mass flow rate ($\dot{m}_l$), are analysed using the selected ML-model and the results are shown in Figs. 11 to 14. Fig. 11(a) depicts the primary breakup length (l_s) as a function of momentum flux ratio along with the axial (l_x) and radial jet penetration (l_r). Fig. 11(b) indicates the same for different values of air crossflow velocity and fuel mass flow rate. As observed from previous studies (Birouk et al., 2003; Ragucci et al., 2007) it can be also seen from Fig. 11(a) that the breakup length increases with momentum flux ratio. The effect of the crossflow velocity variation on l_s is more diverse and depends on the liquid jet Reynolds number. For the u_b-variation from 65 to 133 m/s at $\dot{m}_l = 0.50$ g/s (i.e., low Re_l), the breakup length decreases with increasing u_b by more than 30%. At low Re_l, the enhanced crossflow velocity leads to elevated jet bending, see also the plots of l_x and l_r in Fig. 11, and advance jet breakup. For the interim case with $\dot{m}_l = 1.0$ g/s, the length of the unrolled jet surface on

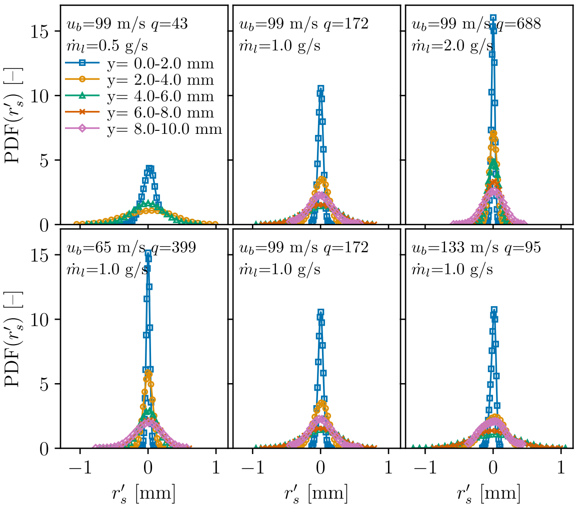

Fig. 12. Normalised probability density functions (PDFs) of the turbulent GLI fluctuation (r'_s) for JiCF sprays. The top row illustrates the influence of different fuel mass flow rates ($\dot{m}_l$), with panels arranged (from left to right) as cases JiCF4J, JiCF5J, and JiCF6J. The bottom row shows the effect of varying air crossflow velocities (u_b), for panels arranged (from left to right) as JiCF2J, JiCF5J, and JiCF8J. In all cases, q represents the momentum flux ratio.

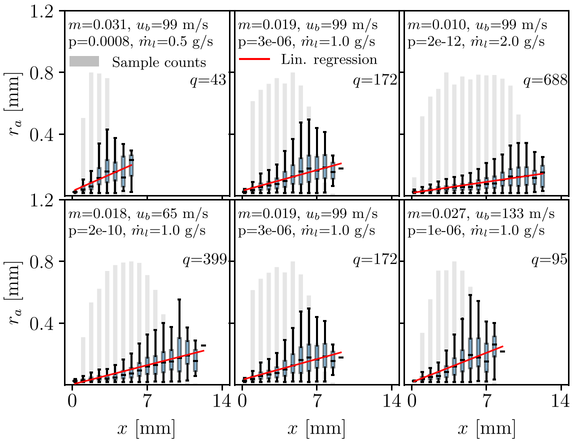

Fig. 13. Mean (marker) and rms (bars) of the GLI disturbance amplitudes (r_a) for JiCF sprays. The top row illustrates the influence of different fuel mass flow rates ($\dot{m}_l$), with panels arranged (from left to right) as cases JiCF4J, JiCF5J, and JiCF6J. The bottom row shows the effect of varying air crossflow velocities (u_b), for panels arranged (from left to right) as JiCF2J, JiCF5J, and JiCF8J. In all cases, q represents the momentum flux ratio. The solid line shows the fitted regression model with a slope m.

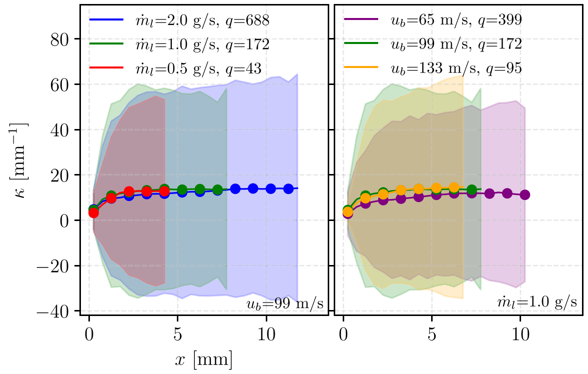

Fig. 14. Mean GLI curvature ($\overline{\kappa}$) along the axial fuel jet penetration direction (x) for JiCF sprays for different fuel mass flow rates ($\dot{m}_l$) (left with cases JiCF4J, JiCF5J and JiCF6J) and air crossflow velocities (u_b) (right with cases JiCF2J, JiCF5J and JiCF8J). The shaded area illustrates the curvature fluctuation (κ').

the luv side varies only within 5%. Thus, the reduced length of the jet core is approximately balanced by the enhanced jet surface wrinkling. By contrast, at $\dot{m}_l = 2.0\,\text{g/s}$ with high Re_l and thus momentum flux ratio, the breakup length increases with u_b by almost 20%. At high Re_l, the trend reversion is attributed to enhanced fuel jet surface wrinkling as also shown by the elevated curvature statistics in Fig. 14.

The bulk motion of the fuel jet is illustrated in Fig. 12 by means of the probability density function of the spatial GLI displacement fluctuation (PDF(r'_s)). With increasing $\dot{m}_l$, the jet becomes less prone to the turbulent flow motion of the gaseous crossflow as illustrated by the narrowing PDF(r'_s) in the top row of Fig. 12. With increasing axial distance (y) the jet fluctuation increases noticeably for all $\dot{m}_l$ as observed by the enhanced spread of PDF(r'_s). As expected, an increase in air crossflow bulk velocity results in enhanced spatial turbulent jet fluctuations (Birouk et al., 2003), where differences are more strongly pronounced with increasing injection point distance, see bottom row of Fig. 12.

Fig. 13 illustrates mean and root mean square (rms) values of disturbance amplitudes (r_a, as described in Section 3.3) along the GLI of the jet surface in injection direction (x). Selected cases with varying air crossflow velocity and fuel mass flow rate are shown. As expected, due to the excitation by aerodynamic forces, the perturbations on the GLI increase with distance from the injector orifice. This is indicated by the positive slope of the linear regression as well as the increasing bar height illustrating a higher disturbance variance. With increasing fuel mass flow rate ($\dot{m}_l$, top row of Fig. 13) the growth rate of the GLI disturbances is dampened, yet the jet core penetrates significantly deeper into the crossflow domain. The former is inferred from the reduced slope and the dampened growth from the bar height. Consequently, the disturbances on the GLI surface of a liquid fuel jet with low Re_l is more sensitive to aerodynamic forces of the crossflow. By contrast, an increase in crossflow velocity in the range $65 \leq u_b\,(\text{m/s}) \leq 133$ (see bottom row of Fig. 13) results in disturbance amplitudes being excited more effectively, leading to elevated mean growth rates (i.e., slope increase > 100%) and disturbance amplitude fluctuations (i.e., bar height). This indicates faster growth of Kelvin–Helmholtz instabilities and thereby advanced jet breakup into ligaments and droplets. The p-values in the plots are obtained from the linear regression analysis and tests the null hypothesis that there is no linear relationship between the independent and dependent variables. The low p-values indicate that the observed associations are statistically significant.

Last, the curvature (κ) on the GLI interface is depicted in Fig. 14 and analysed. As evident from the mean curvature illustrated by the markers, it is evident that the difference in jet-bending with increasing $\dot{m}_l$ and thus Re_l exhibits a marginal effect on $\overline{\kappa}$ and is only visible in the first 2.0 mm away from the injector orifice. However, with increasing Re_l the inherent wrinkling of the turbulent jet surface becomes apparent in the prompt increase of GLI curvature fluctuations (widening of the shaded area), at a given position x. This can contribute to the domination of bag breakup at higher liquid jet and crossflow Weber numbers (Birouk et al., 2003). While the disturbance amplitudes (r_a) continuously grow with increasing distance from the injector orifice, the mean curvature and its fluctuation approach a constant value. Moreover, r'_a are noticeably higher for low jet Reynolds numbers, while κ' approaches very similar levels for all $\dot{m}_l$ cases. For the air crossflow velocity variation from $65 \leq u_b\,(\text{m/s}) \leq 133$, slightly stronger differences in $\overline{\kappa}$ are visible. Yet, the strongest effect is also apparent in the curvature fluctuations as illustrated by shaded area, where κ' increases with u_b, in particular with increasing distance from the injector orifice (i.e., $x \geq 5$ mm). Consequently, at high crossflow velocity the disturbance amplitudes, its fluctuation and curvature fluctuations are highest, indicating a highly convoluted GLI surface and strong excitation of instabilities.

Table 5
Summary of breakup length (l_b) and spray angle (Θ_s) for Schlick V121 spray analysis.

Case	l_b [mm]		Θ_s [°]	
	$\overline{\psi}$	ψ'	$\overline{\psi}$	ψ'
S1 W	2.61	0.45	77.3	6.30
S2 W	2.51	0.47	80.3	5.50
S3 W	2.33	0.48	85.2	6.73

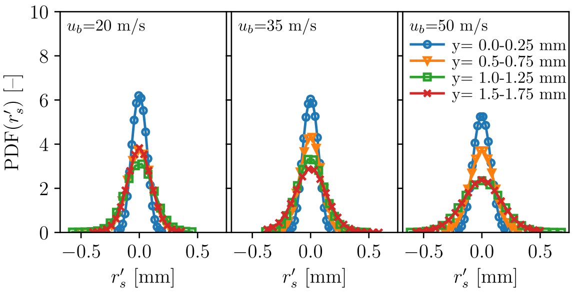

Fig. 15. Normalised probability density function of the turbulent GLI fluctuation (r'_s) of the PS spray sheet at various axial lengths along water injection direction and different bulk flow velocities (u_b).

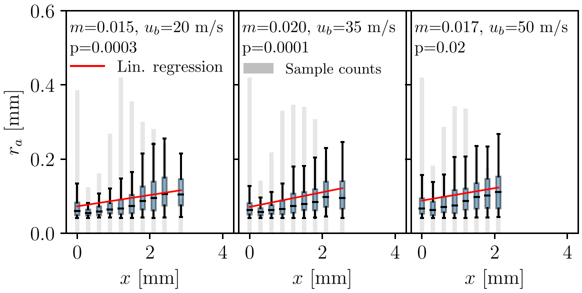

Fig. 16. Mean (marker) and rms (bars) of the GLI disturbance amplitudes (r_a) for PS sprays in water injection direction for different coflow air velocities (u_b). The solid line shows the fitted regression model with a slope m.

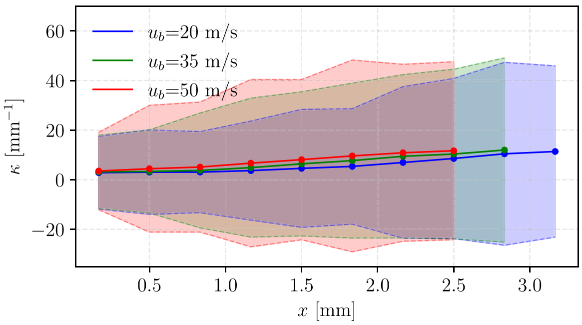

Fig. 17. GLI curvature (κ) along the axial water sheet penetration direction (x) for PS sprays for different air coflow velocities (u_b). The shaded area illustrates the curvature fluctuation (κ').

4.3. *Pressure swirl spray*

In a next step, the ML3 model is applied to segregate the continuous liquid sheet of the PS injector, followed by a statistical analysis on the detected GLI to infer the water spray angle and breakup length, summarised in Table 5, as well as a detailed description of disturbance amplitudes and curvatures. It is evident that with the increase in coflow velocity, the spray angle widens and the breakup length decreases. This is consistent with the algorithm based analysis on the identical sprays conducted by Petry et al. (2022) and with observations in previous studies (Schäfer et al., 2020; Enderle et al., 2018). In this context, it is important to note that the extent of spray angle widening depends on the length of the liquid sheet segment considered in the analysis. In the present study, the linear portion of the liquid sheet spray segment is used. Longer spray segments are more influenced by aerodynamic forces, experience greater bending, and arguably provide a more representative measure of the spray dispersion angle, which directly impacts spatial fuel distribution.

Fig. 15 shows the distribution of the water spray sheet fluctuations at various axial lengths. In the injector orifice proximity, the PDF(r'_s) is rather narrow indicating low fluctuations of thick spray sheets, while the sheet fluctuations increase with axial distance (y) leading to broadened PDF(r'_s). This is particularly prominent for the last segment in the range $1.5 \le y\,(\mathrm{mm}) < 2.0$, where the sheets are thin and most prone to the turbulent fluctuations of the coflowing air. Moreover, as the coflow air velocity is gradually increased from 20 m/s to 50 m/s, the sheet fluctuations are intensified as illustrated by the broadening of PDF(r'_s) for a given axial positions y. This is attributed to the enhanced turbulent intensity of coflowing air.

Fig. 16 shows the mean and rms values of the absolute disturbance amplitudes (r_a) along the water sheet spray surface. It is worth noting that the data in Fig. 15 include the bulk fluctuation of the sheet, while in Fig. 16 the local sheet disturbance (i.e., excited Kelvin–Helmholtz instabilities) are analysed. In general, the disturbances get excited with increasing distance from the injector orifice as shown by the bar height in Fig. 16, yet diminish at the far end. The latter can be attributed to the decreasing number of data points in the corresponding sampling bins and must be treated with care. Moreover, the absolute disturbance amplitudes do not vary significantly between the different cases. This links directly into the constant physical liquid properties and injection momentum (i.e., constant $\dot{m}_l$). Thus, a disturbance of certain amplitude leads to breakup. Nonetheless, the high coflow velocity case (u_b = 50 m/s), and to some degree the case with u_b = 35 m/s, exhibit higher disturbance amplitudes earlier on. This implies that thicker liquid sheet experience stronger instability excitation by the present aerodynamic forces. The reduction in sheet length with increasing u_b, listed in Table 5, is also apparent from the availability of data points in x-direction in Fig. 16. The inclining regression fit indicates the gradual disturbance amplitude growth that is in line with Fig. 15.

The curvature statistics on the water sheet GLI are shown in Fig. 17 for the different coflow velocities (u_b). The mean curvature ($\overline{\kappa}$), shown by the solid lines, is increasing modestly with u_b due to the incremental widening of the spray cone angle. By contrast, the curvature fluctuation is enhanced distinctly with u_b as illustrated be widened shaded area, in particular relatively close to the injector orifice (i.e., low x-values). In combination with the disturbance amplitudes r_a, this shows the existence of relatively high and convoluted disturbance amplitude peaks in the presence of highly turbulent gaseous coflow.

These physical results, except κ-statistics, have broadly been discussed by Petry et al. (2022), yet the repeated analysis using the present Semantic FPN segmentation has shown various benefits to use such ML-based methods for object detection. Firstly, the ML-models have been trained on the JiCF sprays, highlighting the general transferability and applicability of such approaches. Second, in the current work the raw data in absence of any spatial filtering have been used in the analysis. This facilitates the detection of higher disturbance amplitudes in comparison to algorithm CV-based approach by Petry et al. (2022). The latter involved spatial filtering that inherently dampens high frequency peak values. Consequently, the current ML-based image segmentation approach can arguably also maintain the original spatial image resolution to a higher degree and facilitates the inference of a more physical description.

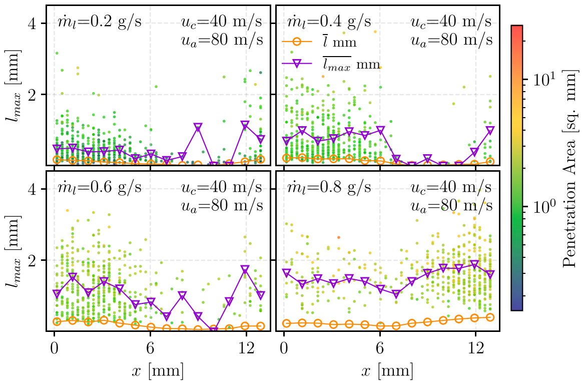

Fig. 18. Scatter plot with cases arranged A10J, A4J (top left to right) and A13J, A15J (bottom left to right) showing the maximum instantaneous penetration depth (l_{max}) of a detached fuel film segment into the gaseous environment for different fuel mass flow rates in the range 0.20 $\leq \dot{m}_l$ (g/s) $\leq$0.80 and constant air flow conditions of u_c = 40 m/s and u_a = 80 m/s. The distribution of the dots illustrates the homogeneity of the l_{max} occurrence along the knife edge, i.e., x-direction. The colour coding of the dots depicts the area of total film detached from the airblast edge of the corresponding instantaneous snapshot. The orange line shows the mean detached film penetration while the purple line shows the mean of the maximum film detachment. (For interpretation of the references to colour in this figure legend, the reader is referred to the web version of this article.)

4.4. Prefilming airblast sprays

Last, the ML3 model is applied to segregate 15 different cases of the prefilming airblast spray and the results of selective cases are analysed and discussed below. In the current context, the detached film is defined as the continuous liquid body downstream from the airblast edge, that is divided into segments by the predefined bins. The scatter plot in Fig. 18 illustrates the relationship between maximum detached film segment lengths of an instantaneous image at position x for varying fuel mass flow rate 0.20 $\leq \dot{m}_l$ (g/s) $\leq$0.80. The area of the detached liquid film is indicated by the colour coding of each sampling point, where each sample point represents a single instantaneous image of the in total 500 images analysed for each case. The film coflow (u_c) and airblast (u_a) air velocities are maintained constant at 40 and 80 m/s, respectively. For all cases, a certain spatial inhomogeneity is observed that is modestly improved with increasing $\dot{m}_l$. The statistical maximum detached film segment penetration depth ($\overline{l_{max}}$, purple line) increases with fuel mass flow rate along with the underlying area of the detached film as illustrated by colour coding. However, while the maximum penetration depth of individual film segments is approximately constant, its occurrence frequency is increasing with $\dot{m}_l$. This allows to infer that in the current setup the atomization and film stripping mechanism are dominated by air shear flow. This is confirmed by separately conducted phase Doppler interferometry (PDI) droplet size measurements (not included here), where the Sauter mean diameter (d_{32}) varies below 10%.

The curvature of the continuous detached liquid fuel film penetrating into the gaseous environment is shown in Fig. 19. With increasing fuel mass flow rate, the mean curvature ($\overline{\kappa}$) increases by ~ 1.1 mm^{-1} with every 0.2 g/s increase in fuel mass flow rate. At the same time, the average curvature fluctuation, i.e., $\overline{\kappa'}$, increases more steeply ~ 3 mm^{-1} towards larger fuel mass flow rates as illustrated by the shaded area. This is attributed to the elevated detached film penetrate depth, where it is exposed to the gaseous flow shear forces leading to a higher curvature on the GLI. It is also worth noting, that the spatial inhomogeneity of the maximum detached film segment distribution and the GLI curvature (compare Figs. 18 and 19) align. This implies that with increasingly detached film segments length, its GLI becomes more wrinkled prior to the formation and breakup into ligaments and droplets.

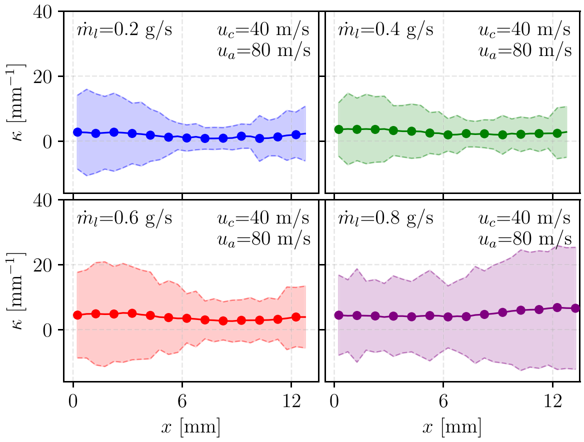

Fig. 19. Curvature (κ) along the gas-liquid-interface in x-direction (i.e., airblast knife edge) with cases arranged A10J, A4J (top left to right) and A13J, A15J (bottom left to right) for different fuel mass flow rates in the range 0.20 $\leq \dot{m}_l$ (g/s) $\leq$0.80 and constant air flow conditions of u_c = 40 m/s and u_a = 80 m/s. The symbols and line shows the mean curvature ($\overline{\kappa}$), while the shaded area illustrates the curvature fluctuation (κ').

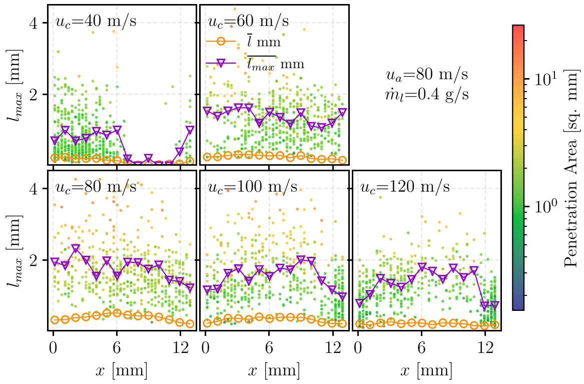

Fig. 20. Scatter plot with cases arranged A4J, A5J (top left to right) and A1J, A6J, A7J (bottom left to right) showing the maximum instantaneous penetration depth (l_{max}) of a detached fuel film segment into the gaseous environment for different air coflow velocities in the range 40 $\leq u_c$ (m/s) $\leq$120 and constant atomization air velocity (u_a = 80 m/s) and fuel mass flow rate ($\dot{m}_l$ = 0.40 g/s). The distribution of the dots illustrates the homogeneity of the l_{max} occurrence along the knife edge, i.e., x-direction. The colour coding of the dots depicts the area of total film detached from the airblast edge of the corresponding instantaneous snapshot. The orange line shows the mean detached film penetration while the purple line shows the mean of the maximum film detachment. (For interpretation of the references to colour in this figure legend, the reader is referred to the web version of this article.)

Similar to Fig. 18, Fig. 20 illustrates the relationship between maximum detached fuel film segment penetration depth for varying air coflow velocity from 40 $\leq u_c$ (m/s) $\leq$120. The airblast velocity is maintained at u_a = 80 m/s and the fuel mass flow rate at $\dot{m}_l$ = 0.40 g/s. With increasing u_c the statistical penetration depth first increases up to u_c = u_a = 80 m/s and then decreases modestly as illustrated by the vertical translation of the purple line. The same trend holds for the mean film penetration (orange line) and thereby also the area of the detached fuel film. It is also worth noting that the spatial homogeneity follows the same behaviour, where inhomogeneous distributions are observed for the two limiting cases.

Fig. 21 shows the curvature statics of the GLI for the corresponding u_c variation. Once more, detached fuel films penetrating deeper into the gaseous flow environment become more wrinkled, with the highest curvature and fluctuation observed for in the case u_c = u_a = 80 m/s. Albeit this case exhibits no nominal shear, the turbulent intensity of the individual gas streams cause the observed GLI wrinkling with high curvature fluctuation. Increasing the aerodynamic shear forces leads

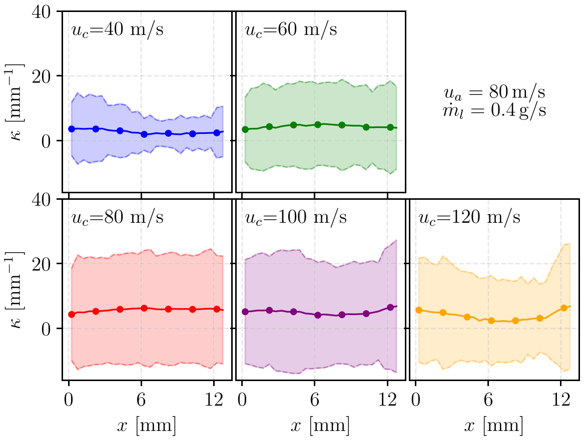

Fig. 21. Curvature (κ) along the gas-liquid-interface in x-direction (i.e., airblast knife edge) with cases arranged A4J, A5J (top left to right) and A1J, A6J, A7J (bottom left to right) for different air coflow velocities in the range $40 \leq u_c\,(\mathrm{m/s}) \leq 120$ and constant atomization air velocity ($u_a = 80\,\mathrm{m/s}$) and fuel mass flow rate ($\dot{m}_l = 0.40\,\mathrm{g/s}$). The symbols and line shows the mean curvature ($\overline{\kappa}$), while the shaded area illustrates the curvature fluctuation (κ').

to advanced film breakup, thereby reducing the detached fuel film penetration depth of segments with reduced curvature. It is further worth noting, that both ligament and bag breakups are observed in all cases, while ligament breakup is more prominent in cases where the fuel mass flow rate and coflow air velocity are both low. This coincides with previous studies on airblast sprays (Chaussonnet et al., 2018). Moreover, fragmented detached films with deep penetration and high curvature are not necessarily advantageous for atomization into fine droplets. For the latter, high shear between u_a and u_c is arguably the driving force, while a minimum coflow velocity is required to augment the film distribution on the airblast wall.

5. Conclusions

The overarching objective of the current work is to develop and apply a general applicable and transferable semantic segmentation model without parameter tuning to segregate the shadowgraphy signal of technical sprays from the gaseous background. Thereby, the present ML-based image segmentation replaces conventional thresholding methods for creating binary masks. For this purpose, two different training datasets and machine learning architectures are evaluated. The models are trained on one specific kind of spray, yet the selected model ML3 is able to accurately generalise to unknown spray types. Automatic annotation methods are applied, thereby reducing the corresponding effort which is a major bottleneck in most ML pipelines. The best performing ML model, based on the Semantic FPN architecture, is subsequently integrated to an in-house data analysis framework and used to analyse shadowgraphy data of jet-in-crossflow, pressure swirl and prefilming airblast sprays.

The transferability of the ML segmentation model across different spray configurations without parameter tuning has been demonstrated successfully. This offers a distinct reduction in the post-processing time of experimental shadowgraphy images. Moreover, the accuracy of the extracted spray contours in absence of spatial filtering facilitates the delineation of high-level statistical properties such as curvature, fragmentation, and growth of Kelvin–Helmholtz instabilities along gas-liquid-interfaces on an instantaneous image basis. This allows to provide a quantitative description of the involved turbulence-spray interactions and the leading mechanism causing primary breakup of liquid jets, sheets or films. Consequently, it is expected that the present data can provide a valuable validation set for numerical simulation that target primary atomization of technical sprays at high Reynolds number. With minimal effort, the presented segmentation techniques can also be extended to other optical spray measurement techniques that aim to isolate spray contours, including advanced X-ray diagnostics (MacPhee et al., 2002; Mayhew et al., 2020; Tekawade et al., 2020). Applying this method allows a precise isolation of the dense spray core and a subsequent quantitative description of the breakup processes.

Although the model accurately segments raw data, some artefacts as discussed before are visible. While the number of such aberrations is not significant to statistically skew the results of the present study, great care must be taken when using such models as black box, in particular for datasets where the number of data points is scarce. Related effects can arguably be mitigated, for example, by using advanced augmentations in addition to the steps applied here, reinforcement learning, or case-dependent and in-situ parameter tuning, which is subject to future work.

CRediT authorship contribution statement

Basil Jose: Writing – review & editing, Writing – original draft, Visualization, Software, Methodology, Investigation, Formal analysis, Conceptualization. **Oliver Lammel:** Resources, Funding acquisition. **Fabian Hampp:** Writing – review & editing, Writing – original draft, Supervision, Resources, Project administration, Funding acquisition, Data curation, Conceptualization.

Declaration of competing interest

The authors declare the following financial interests/personal relationships which may be considered as potential competing interests: Fabian Hampp reports financial support was provided by German Research Foundation. If there are other authors, they declare that they have no known competing financial interests or personal relationships that could have appeared to influence the work reported in this paper.

Acknowledgements

This work was funded by the Deutsche Forschungsgemeinschaft (DFG, German Research Foundation) - project number: 456687251. The experimental data have been acquired during the project (FL)^2 Flüssig FLOX, Programmdirektion Energie, German Aerospace Center. We further acknowledge the support by the Stuttgart Center for Simulation Science (SimTech).

Appendix A. Supplementary data

Supplementary material related to this article can be found online at https://doi.org/10.1016/j.ijmultiphaseflow.2025.105179.

Data availability

The database and selected ML model (ML3) is available on the IVLR Data Repository of the University of Stuttgart (DaRUS) https://doi.org/10.18419/DARUS-4739.

References

Acharya, P., Burgers, T., Nguyen, K.-D., 2023. A deep-learning framework for spray pattern segmentation and estimation in agricultural spraying systems. Sci. Rep. 13, 7545.

Anderson, D., Smith, J., Brown, E., 2020. Lowest emission sustainable aviation biofuels as the potential replacement for the jet-a fuels. Aircr. Eng. Aerosp. Technol. 92, 345–356.

Birouk, M., Azzopardi, B., Stäbler, T., 2003. Primary break-up of a viscous liquid jet in a cross airflow. Part. Syst. Charact. 20, 283–289.

Bradski, G.R., 1998. Computer vision face tracking for use in a perceptual user interface. Intel Technol. J.

Chaussonnet, G., Laroche, T., Lieber, C., Holz, S., Koch, R., Bauer, H.-J., 2018. Investigation of the liquid accumulation characteristics in planar prefilming airblast atomization. In: Proc. 14th Int. Conf. Liq. Atomiz. & Spray Systems. ICLASS2018, Chicago, IL, July 22–26, 34.14.02; LK 01.

Chen, L.-C., Papandreou, G., Kokkinos, I., Murphy, K., Yuille, A.L., 2017a. Deeplab: Semantic image segmentation with deep convolutional nets, atrous convolution, and fully connected crfs. arXiv:1606.00915.

Chen, L.-C., Papandreou, G., Schroff, F., Adam, H., 2017b. Rethinking atrous convolution for semantic image segmentation. arXiv:1706.05587.

Chen, L.-C., Zhu, Y., Papandreou, G., Schroff, F., Adam, H., 2018. Encoder–decoder with atrous separable convolution for semantic image segmentation. arXiv:1802.02611.

Chong, W.T., Hochgreb, S., 2014. Spray characteristics of an internal-mix airblast atomizer. Appl. Mech. Mater. 629, 125–130.

Chong, W.T., Hochgreb, S., Wong, T., 2012. Flow field of a model gas turbine swirl burner. Adv. Mater. Res. 622–623, 1119–1124.

Chun-Yu, G., Yi-Wei, F., Yang, H., Peng, X., Yun-Fei, K., 2021. Deep-learning-based liquid extraction algorithm for particle image velocimetry in two-phase flow experiments of an object entering water. Appl. Ocean Res. 108, 102526.

Cordts, M., Omran, M., Ramos, S., Rehfeld, T., Enzweiler, M., Benenson, R., Franke, U., Roth, S., Schiele, B., 2016. The cityscapes dataset for semantic urban scene understanding. In: Proc. IEEE Comput. Soc. Conf. Comput. Vis. Pattern Recognit.

Deng, J., Dong, W., Socher, R., Li, L.-J., Li, K., Fei-Fei, L., 2009. ImageNet: A large-scale hierarchical image database. In: Proc. IEEE Comput. Soc. Conf. Comput. Vis. Pattern Recognit.. pp. 248–255.

Enagi, A., Kato, Y., Takahashi, Y., Matsumoto, T., 2019. Liquid fuels spray and combustion characteristics in a new micro gas turbine combustion chamber design. Int. J. Energy Res. 43, 123–135.

Enderle, B., Grimm, F., Rauch, B., Aigner, M., Chaussonnet, G., 2018. Derivation and numerical study of spray boundary conditions for a pressure swirl atomizer issuing into co-flowing air. In: Proc. Glob. Power Propuls. Soc.

Fansler, T.D., Parrish, S.E., 2015. Spray measurement technology: a review. Meas. Sci. Technol. 26, 012002.

Godbehere, A.B., Matsukawa, A., Goldberg, K., 2012. Visual tracking of human visitors under variable-lighting conditions for a responsive audio art installation. In: IEEE ACC. pp. 4305–4312.

Großkopf, J., Matthes, J., Vogelbacher, M., Waibel, P., 2021. Evaluation of deep learning-based segmentation methods for industrial burner flames. Energies 14.

Halevy, A., Norvig, P., Pereira, F., 2009. The unreasonable effectiveness of data. IEEE Intell. Syst. 24, 8–12.

Hampp, F., Lindstedt, R.P., 2017. Quantification of combustion regime transitions in premixed turbulent DME flames. Combust. Flame 182, 248–268.

Hampp, F., Schäfer, D., Lammel, O., 2023. Spray flame characterization of a dual injector for compact combustion systems. Combust. Sci. Technol. 1–34.

He, K., Gkioxari, G., Dollár, P., Girshick, R., 2020. Mask R-CNN. IEEE Trans. Pattern Anal. Mach. Intell. 42, 386–397.

He, X., Liao, L., Zhang, H., Nie, L., Hu, X., Chua, T.-S., 2017. Neural collaborative filtering. arXiv:1708.05031.

He, K., Sun, J., Tang, X., 2010. Single image haze removal using dark channel prior. IEEE TPAMI 33, 2341–2353.

He, Y., Wang, H., Zhang, B., 2004. Color-based road detection in urban traffic scenes. IEEE Trans. Intell. Transp. Syst. 5, 309–318.

Ho, J., Jain, A., Abbeel, P., 2020. Denoising diffusion probabilistic models. arXiv:2006.11239.

Hoover, A., Kouznetsova, V., Goldbaum, M., 2000. Locating blood vessels in retinal images by piecewise threshold probing of a matched filter response. IEEE Trans. Med. Imaging 19, 203–210.

Hu, F., Zhou, M., Yan, P., Bian, K., Dai, R., 2019. PCAnet: A common solution for laser-induced fluorescence spectral classification. IEEE Access 7, 107129–107141.

Huzjan, F., Jurić, F., Lončarić, S., Vujanović, M., 2023. Deep learning-based image analysis method for estimation of macroscopic spray parameters. Neural Comput. Appl. 35, 9535–9548.

Jose, B., Hampp, F., 2024. Machine learning based spray process quantification. Int. J. Multiph. Flow 172, 104702.

Kaewtrakulpong, P., Bowden, R., 2002. An improved adaptive background mixture model for realtime tracking with shadow detection. In: Video-Based Surveillance Systems. Springer US.

Kang, Y., Ahn, J., Hampp, F., 2024. Low swirl effect on compact spray and combustion systems using additive manufactured dual airblast injectors. J. Eng. Gas Turb. Power 146, GTP–24–1281.

Kapur, J.N., Sahoo, P.K., Wong, A.K.C., 1985. A new method for gray-level picture thresholding using the entropy of the histogram. Comput. Vis. Graph. Image Process. 29, 273–285.

Kirillov, A., Girshick, R., He, K., Dollár, P., 2019. Panoptic feature pyramid networks. arXiv:1901.02446.

Kirillov, A., Wu, Y., He, K., Girshick, R., 2020. Pointrend: Image segmentation as rendering. In: Proc. IEEE Comput. Soc. Conf. Comput. Vis. Pattern Recognit. IEEE Computer Society, Los Alamitos, CA, USA, pp. 9796–9805.

Kober, J., Bagnell, J.A., Peters, J., 2013. Reinforcement learning in robotics: A survey. Int. J. Robot. Res. 32, 1238–1274.

Koyama, H., Tachibana, M., 2012. Technical applicability of low-swirl fuel nozzle for a liquid-fueled industrial gas turbine combustor. J. Gas Turb. Eng. 134, 68662.

Krizhevsky, A., Sutskever, I., Hinton, G.E., 2012. ImageNet classification with deep convolutional neural networks. Adv. Neural Inf. Process. Syst. 25.

Lefebvre, A.H., McDonell, V.G., 2017. Atomization and Sprays, second ed. CRC Press.

Li, J., Bioucas-Dias, J.M., Plaza, A., 2010. Semisupervised hyperspectral image segmentation using multinomial logistic regression with active learning. IEEE Trans. Geosci. Remote Sens. 48, 4085–4098.

Lin, T.-Y., Dollár, P., Girshick, R., He, K., Hariharan, B., Belongie, S., 2017. Feature pyramid networks for object detection. arXiv:1612.03144.

Lindman, O., Andersson, M., Persson, M., Erik, M., 2014. Development of a liquid fuel combustion system for SGT-750. In: Proc. ASME Turbo Expo, vol. 6, GT2014–25380.

MacPhee, A.G., Tate, M.W., Powell, C.F., Yue, Y., Renzi, M.J., Ercan, A., Narayanan, S., Fontes, E., Walther, J., Schaller, J., Gruner, S.M., Wang, J., 2002. X-ray imaging of shock waves generated by high-pressure fuel sprays. Science 295, 1261–1263.

Mayhew, E., Wood, E., McGann, B., Mitsingas, C., Oldani, A., Rajasegar, R., Temme, J., Kweon, C.-B., Matusik, K., Kastengren, A., Lee, T., 2020. High-speed phase contrast imaging of spray breakup of jet fuels under combusting conditions. At. Sprays 31.

Molière, M., 2023. The fuel flexibility of gas turbines: A review and retrospective outlook. Energies 16, 3962.

Moon, S., Abo-Serie, E., Bae, C., 2009. Air flow and pressure inside a pressure-swirl spray and their effects on spray development. Exp. Therm. Fluid Sci. 33, 222–231.

Oshima, I., A., S., 2019. Longitudinal oscillation of a liquid sheet by parallel air flows. Int. J. Multiph. Flow 110, 179–188.

Otsu, N.A., 1979. Threshold selection method from grey-level histograms. IEEE Trans. Syst. Man. Cybern. 8, 62–66.

Packard, R.R.S., Baek, K.I., Beebe, T., Jen, N., Ding, Y., Shi, F., Fei, P., Kang, B.J., Chen, P.-H., Gau, J., Chen, M., Tang, J.Y., Shih, Y.-H., Ding, Y., Li, D., Xu, X., Hsiai, T.K., 2017. Automated segmentation of light-sheet fluorescent imaging to characterize experimental doxorubicin-induced cardiac injury and repair. Sci. Rep. 7, 8603.

Pérez-Guerrero, C., Palacios, A., Ochoa-Ruiz, G., Foroughi, V., Pastor, E., Gonzalez-Mendoza, M., Falcón-Morales, L.E., 2022. Experimental large-scale jet flames' geometrical features extraction for risk management using infrared images and deep learning segmentation methods. J. Loss Prev. Process. Ind. 80, 104903.

Pesaresi, M., Benediktsson, J., 2001. A new approach for the morphological segmentation of high-resolution satellite imagery. IEEE Trans. Geosci. Remote Sens. 39, 309–320.

Petry, N., Schäfer, D., Lammel, O., Hampp, F., 2022. Quantification of coflow effects on primary atomization of pressure swirl atomizers. Int. J. Multiph. Flow 149, 103946.

Raghu, A., Karthikeyan, S., Venkatesh, R., Ramesh, A., 2015. Spray characteristics of diesel and biodiesel fuels for various injection timings under non evaporating conditions. Appl. Mech. Mater. 787, 682–688.

Ragucci, R., Bellofiore, A., Cavaliere, A., 2007. Breakup and breakdown of bent kerosene jets in gas turbine conditions. Proc. Combust. Inst. 31, 2231–2238.

Redmon, J., Divvala, S., Girshick, R., Farhadi, A., 2016. You only look once: Unified, real-time object detection. arXiv:1506.02640.

Schäfer, D., Hampp, F., Lammel, O., Aigner, M., 2020. Investigation of spray formation and turbulent droplet transport in high momentum jet stabilized combustor injection systems. In: Volume 4B: Combustion, Fuels, and Emissions of Turbo Expo: Power for Land, Sea, and Air.

Sotelo, M.A., Rodriguez, F.J., Magdalena, L., Bergasa, L.M., Boquete, L., 2004. A color vision-based lane tracking system for autonomous driving on unmarked roads. Auton. Robots 16, 95–116.

Stefanizzi, M., Bianchi, G., Cattaneo, A., Mariani, A., 2021. Recent combustion strategies in gas turbines for propulsion and power generation toward a zero-emissions future: Fuels, burners, and combustion techniques. Energies 14, 1–20.

Stöhr, M., Ruoff, S., Rauch, B., Meier, W., Le Clercq, P., 2021. Droplet vaporization for conventional and alternative jet fuels at realistic temperature conditions: Systematic measurements and numerical modeling. Proc. Combust. Inst. 38, 3269–3276.

Strässle, R.M., Faldella, F., Doll, U., 2024. Deep learning-based image segmentation for instantaneous flame front extraction. Exp. Fluids 65, 94.

Sun, C., Shrivastava, A., Singh, S., Gupta, A., 2017. Revisiting unreasonable effectiveness of data in deep learning era. arXiv:1707.02968.

Szeliski, R., 2022. Computer Vision: Algorithms and Applications. Springer Nature.

Tekawade, A., Sforzo, B., Matusik, K., Fezzaa, K., Kastengren, A., Powell, C., 2020. Time-resolved 3D imaging of two-phase fluid flow inside a steel fuel injector using synchrotron X-ray tomography. Sci. Rep. 10.

Touvron, H., Lavril, T., Izacard, G., Martinet, X., Lachaux, M.-A., Lacroix, T., Rozière, B., Goyal, N., Hambro, E., Azhar, F., Rodriguez, A., Joulin, A., Grave, E., Lample, G., 2023. Llama: Open and efficient foundation language models. arXiv:2302.13971.

Urbán, A., Katona, B., Malý, M., Jedelský, J., Józsa, V., 2020. Empirical correlation for spray half cone angle in plain-jet airblast atomizers. Fuel 277, 118197.

Vaithiyanathan, M., Safa, N., Melvin, A.T., 2019. FluoroCellTrack: An algorithm for automated analysis of high-throughput droplet microfluidic data. PLoS One 14, 1–22.

Zhang, Y., Brady, M., Smith, S., 2001. Segmentation of brain mr images through a hidden markov random field model and the expectation–maximization algorithm. IEEE Trans. Med. Imaging 20, 45–57.